Formation and Transformation Kinetics of Amorphous Iron(III) Oxide during the Thermally Induced Transformation of Ferrous Oxalate Dihydrate in Air

Nobuyoshi Koga* and Yuka Sato

Chemistry Laboratory, Department of Science Education, Graduate School of Education, Hiroshima University, 1-1-1 Kagamiyama, Higashi-Hiroshima 739-8524, Japan

Received: October 31, 2010; Revised Manuscript Received: December 2, 2010

Focusing on the formation and transformation of amorphous Fe_2O_3 in the course of the thermally induced transformations of ferrous oxalate dehydrate in air, the kinetics and physico-geometric mechanisms of the respective reaction steps were investigated systematically by means of thermoanalytical methods, complemented by other techniques. The final product of α-Fe_2O_3 is produced by heating the sample to 700 K via intermediates of poorly crystalline anhydrous FeC_2O_4 and amorphous Fe_2O_3, where the external shape and size of the original sample particles are retained during the overall course of reactions. The initial parts of all the three distinguished reaction steps, that is, thermal dehydration of crystalline water, oxidative decomposition of anhydrous FeC_2O_4 and crystallization of amorphous Fe_2O_3, are controlled kinetically by the formation or reconstruction of the surface product layers. The surface product layers play important roles of regulating the physico-geometric kinetic behavior of the established parts of the reactions. The oxidative decomposition of intermediate anhydrous FeC_2O_4, characterized as the formation process of amorphous Fe_2O_3, arrests in the final stage of the reaction. The as-produced amorphous Fe_2O_3, protected probably by the outer shell of the surface product layer and the residual anhydrous FeC_2O_3, crystallizes to α-Fe_2O_3 being induced by the surface crystallization. Aiming to contribute notably toward provision of the establishment of the novel fabrication routes of nanosized iron oxides by the controlled crystallization of amorphous Fe_2O_3, the possible factors controlling and/or affecting the formation and transformation kinetics of amorphous Fe_2O_3 were discussed.

1. Introduction

Nanosized particles of iron oxides have various potential utilities of industrial applications due to their catalytic activities, magnetic properties, chemical reactivity, and so on.[1] In order to fabricate the iron oxides with desired size, morphology, and physicochemical property, various wet chemical methods including the biomimetic mineralization processes have been examined.[2,3] At the same time, it is well-known that the thermal decompositions of iron compounds are possible routes to prepare the nanosized particles of iron oxides. A wide range of thermal decompositions of iron compounds has been examined for characterizing the formation kinetics and structural and physicochemical properties of the products, that is, iron oxides.[4−8] Among others, the thermal decomposition of ferric oxalate dihydrate, $FeC_2O_4 \cdot 2H_2O$, has been studied by many workers as the probable route to prepare the nanosized iron(III) oxide polymorphs.[9−23] The reaction pathway of the thermally induced transformations of the compound changes drastically depending on the reaction atmosphere and heating conditions.[10] In an inert gas, reducing gas or self-generated gaseous atmosphere, the reaction mechanisms are very complicated and the final solid products of the thermally induced transformation vary sensitively with the reaction conditions.[14,17,21] The reaction pathway in an oxidizing atmosphere such as in flowing air is rather well-defined, which produces α-Fe_2O_3 via poorly crystalline or amorphous Fe_2O_3 produced by the partially overlapped reactions of thermal dehydration of crystalline hydrate and the oxidative decomposition of dehydrated FeC_2O_4.[20,22,23] Recently, the nanocrystallization of α-Fe_2O_3 from amorphous Fe_2O_3 was illustrated clearly by following the changes of the powder X-ray diffraction (XRD) pattern and transmission electron microscopy (TEM) image by Hermanek et al.[22]

From the viewpoint of reaction kinetics, it is of great interest how the thermodynamically metastable phase of amorphous Fe_2O_3 is stabilized in the course of the thermally induced transformation of $FeC_2O_4 \cdot 2H_2O$ in oxidizing atmosphere. Although it is expected from the previous studies[20,22,23] that the formation reaction of amorphous Fe_2O_3 is the oxidative decomposition of anhydrous FeC_2O_4 under isothermal heating at around 450 K and under linearly increasing temperature in an oxidizing atmosphere, the detailed analyses of the kinetics and physico-geometric mechanism of the formation process have not been carried out. Because the formations of nanoparticles of different iron oxides have been reported as the final solid products of the thermal treatments of $FeC_2O_4 \cdot 2H_2O$ in different atmospheric conditions,[9−23] the controlled crystallizations of nanosized iron oxides from amorphous Fe_2O_3 is highly expected by controlling the transformation kinetics under different atmospheric and heating conditions. In this respect, the fundamental understanding on the transformation kinetics of amorphous Fe_2O_3 to α-Fe_2O_3 on heating in an oxidizing atmosphere is also required as the basis for the controlled crystallization of different iron oxides. In the present study, the kinetic behaviors of the respective reaction steps of the thermally induced transformation of $FeC_2O_4 \cdot 2H_2O$ in air were investigated systematically by means of thermoanalytical measurements after reinvestigating the reaction pathway complemented by other techniques such as high temperature XRD, Fourier transform IR (FT-IR), scanning electron microscopy (SEM) observation and so on. Aiming to contribute notably toward provision of

* To whom correspondence should be addressed. Tel/Fax: +81-82-424-7092. E-mail: nkoga@hiroshima-u.ac.jp.

10.1021/jp110407n
Published on Web 12/15/2010

the establishment of the novel fabrication routes of nanosized iron oxides by the controlled crystallization of amorphous Fe_2O_3, the possible factors controlling and/or affecting the formation and transformation kinetics of the amorphous Fe_2O_3 are discussed on the basis of the present experimental findings complemented by those from the previous works.

2. Experimental Section

2.1. Sample Preparation. An aqueous solution of ammonium iron(II) sulfate (0.1 mol dm^{-3}) was titrated with an aqueous solution of potassium oxalate (0.1 mol dm^{-3}) at a rate of 1.0 cm^3 min^{-1} at 298 K until the pH of mother liquor to be 7. The precipitates produced during the titration were filtered and washed repeatedly with distilled water. The filtrate was dried in a vacuum desiccator for more than 24 h. The sample thus prepared was identified by the powder XRD (RINT2200 V, Rigaku Co., monochrome Cu-K_α, 40 kV, 20 mA) and FT-IR spectroscopy (FTIR8400S, Shimadzu Co., diffuse reflectance method). The morphology of the sample particles was observed by SEM (JSM-6510, Jeol) after coated the sample by Pt evaporation.

2.2. Characterization of Reaction Pathway. Using an instrument of thermogravimetric-differential thermal analysis (TG-DTA) (TG8120, Rigaku Co.) connected to a quadrupole mass-spectrometer (M-200QA, Anelva Co.), TG/DTA-MS measurements in flowing simulated air, that is, 20% oxygen in He, (200 cm^3 min^{-1}) were carried out for about 3.0 mg of the sample weighed into a platinum pan (5 mmϕ and 2.5 mm in height) at a heating rate $\beta = 10$ K min^{-1} where the mass spectra of the evolved gases were recorded in the range from 10 to 50 amu (EMSN, 1.0 A; SEM, 1000 V). Transformations of the solid phases during heating in flowing air were traced by XRD using the above diffractometer equipped with a programmable heating chamber (PTC-20, Rigaku Co.). By heating the sample press-fitted on a platinum plate at 10 K min^{-1}, the diffraction measurements were started at various selected temperatures, where the sample temperature was kept constant during the diffraction measurements for about 15 min. The time-resolved XRD measurements at two selected temperatures were also performed in order to follow the respective reaction steps of thermal dehydration of the crystalline hydrate and the oxidative decomposition of anhydrous FeC_2O_4. FT-IR spectra and SEM images of the intermediate and final products of the thermally induced transformation were also recorded after cooling the sample to room temperature.

2.3. Kinetic Measurements. The respective reaction steps of the thermally induced transformation of the sample, that is, the thermal dehydration of dihydrate, oxidative-decomposition of anhydrate, and crystallization of α-Fe_2O_3 from amorphous Fe_2O_3, were subjected to the kinetic study. The mass-loss traces for the thermal dehydration process were recorded isothermally to avoid the overlapping with the subsequent oxidative decomposition of the intermediate anhydrous FeC_2O_4. In the instrument of TG-DTA (DTG-50, Shimadzu Co.), about 10.0 mg of the sample weighed into a platinum cell (6 mmϕ and 3 mm in height) were heated at constant temperatures from 383 to 403 K in flowing air (80 cm^3 min^{-1}).

After dehydrating the sample of 10.0 mg by heating at 403 K for 150 min under the same condition with the above isothermal measurements, the subsequent process of oxidative decomposition of anhydrous FeC_2O_4 in flowing air was traced at selected constant temperatures from 453 to 468 K and at different β from 1 to 5 K min^{-1}. To follow the oxidation of Fe(II) ion to Fe(III) ion in the solid state during the oxidative decomposition step, the sample of 100 mg spread in an alumina boat was heated in a tube furnace at 468 K for different time under the condition otherwise identical with the above isothermal measurements of the mass-loss step of the oxidative decomposition. The samples heated for different times were dissolved in 20 cm^3 of 1.0 mol dm^{-3} HCl under ice cooling and diluted to 50 cm^3 using a measuring flask. Using a portion of the sample solutions, the concentration of Fe(III) ion was determined by the colorimetric method of Fe(III)-salicylic acid complex formation using a UV−vis spectrophotometer (UVmini-1240, Shimadzu Co.). The total concentration of Fe(II) and Fe(III) ions was determined by the same method after oxidizing Fe(II) ion by adding 10 wt % H_2O_2 aq. The fractional oxidations at different heating times were evaluated by the ratio of molar concentration of Fe(III) ion to the total molar concentration of Fe(II) and Fe(III) ions.

An exothermic process observed at the end of oxidative decomposition, separately from the main reaction process, was subjected to DSC measurements. In an instrument of DSC (DSC-60, Shimadzu), the sample of 10.0 mg in the platinum cell (6 mmϕ and 3 mm in height) was heated isothermally at 473 K for 60 min in flowing air (80 cm^3 min^{-1}) in order to complete the mass-loss process of oxidative decomposition. The sample was subsequently heated at different β from 7 to 20 K min^{-1} for recording DSC exothermic peak.

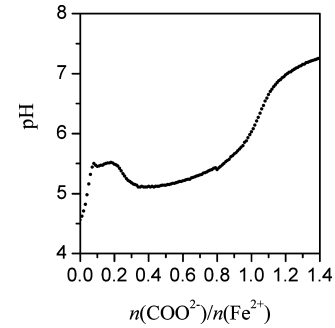

Figure 1. pH titration curve for the precipitation reaction of $FeC_2O_4 \cdot 2H_2O$.

3. Results and Discussions

3.1. Characterizations of the Sample and Its Thermal Behavior in Air. During the titration of $Fe(NH_4)_2(SO_4)_2$ aq by $K_2C_2O_4$ aq characterized by the pH titration curve shown in Figure 1, yellow crystalline precipitates were obtained in the pH range from 5 to 7. Because the preparation conditions influence largely on the morphology and size of the precipitated particles of $FeC_2O_4 \cdot 2H_2O$[23] and consequently on the details of the kinetics of the thermally induced transformation, the pH titration curve in Figure 1 was represented as the reference of the present sample preparation. Figure 2 shows the powder XRD pattern and the FT-IR spectrum of the as-precipitated sample. All the XRD peaks shown in Figure 2a were indexed to those of $FeC_2O_4 \cdot 2H_2O$ of orthorhombic phase.[24] The IR spectrum, Figure 2b, indicates the O−H stretching band at 3319 cm^{-1} and typical IR absorption peaks due to oxalate ion and metal−O bond in metal oxalates,[19,25−28] that is, C−O symmetric stretching at 1361, C−O asymmetric stretching at 1651, O−C−O stretching at 1317, O−C−O bending at 822, and Fe−O stretching at 534 cm^{-1}. A typical SEM image of the sample was shown in Figure 3, where the sample particles are characterized as aggregates of quadratic prisms of several micrometers.

Figure 4 shows the typical TG-DTA curves of the sample in flowing simulated air, together with the mass-chromatograms

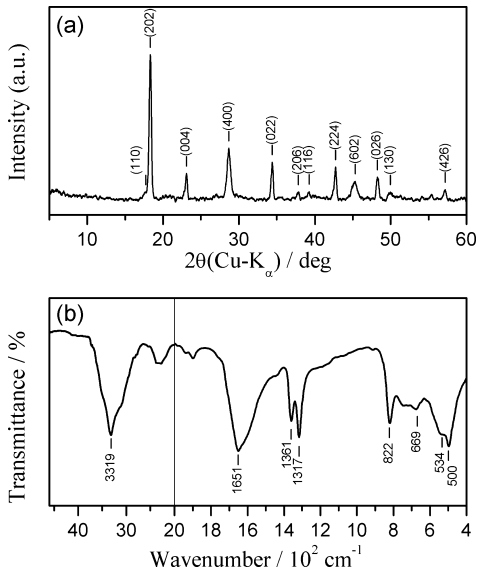

Figure 2. XRD pattern (a) and FT-IR spectrum (b) of $FeC_2O_4 \cdot 2H_2O$.

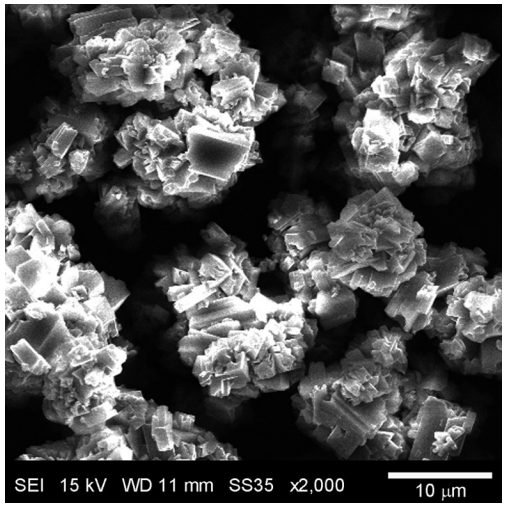

Figure 3. A typical SEM image of $FeC_2O_4 \cdot 2H_2O$.

of m/z18 and m/z44 of the evolved gases. The thermally induced transformation proceeds via three distinguished mass-loss steps. The first mass-loss step is endothermic process, evolving water vapor. The evolution of CO_2 at the final stage of the first mass-loss step is indicating the partial overlapping with the second mass-loss step. The second and third mass-loss steps are exothermic processes, where only CO_2 is detected by the mass spectroscopic measurement of the evolved gas and m/z28 of CO^+ was detected only as the fragment ion of CO_2.

The changes of XRD pattern of the sample during the stepwise isothermal heating in flowing air are represented in Figure 5a. At the temperature corresponding to the end of thermal dehydration, that is, 473 K, a poorly crystalline phase with a distinguished diffraction peak at $2\theta = 23.86°$ appears. By heating the sample to the end temperature of the second mass-loss process, the solid phase changes to nearly amorphous at 523 K. On further heating, the amorphous phase crystallizes during the third mass-loss step of exothermic process. The diffraction peaks appear at 573 K and grow gradually at higher temperatures. Figure 5b shows the XRD pattern of the final decomposition product at 773 K. All the diffraction peaks are indexed to rhombohedral phase of Fe_2O_3, hematite.[29]

Figure 6 compares the IR spectra of the intermediate and final products of the thermally induced transformation. During the

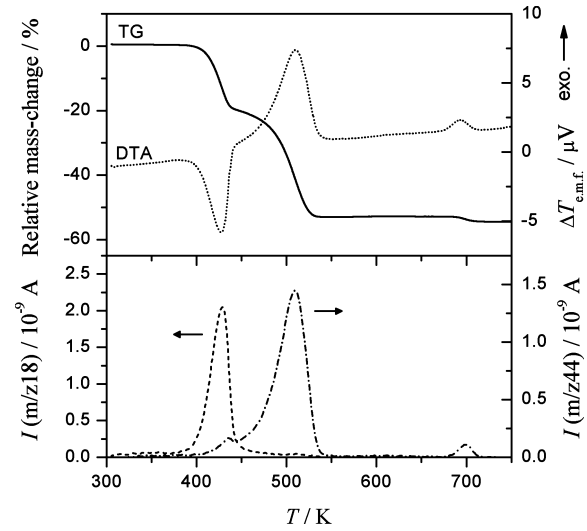

Figure 4. TG-DTA curves of $FeC_2O_4 \cdot 2H_2O$ in flowing simulated air (20% O_2 in He), together with the mass-chromatograms of *m/z*18 and *m/z*44 of the evolved gas.

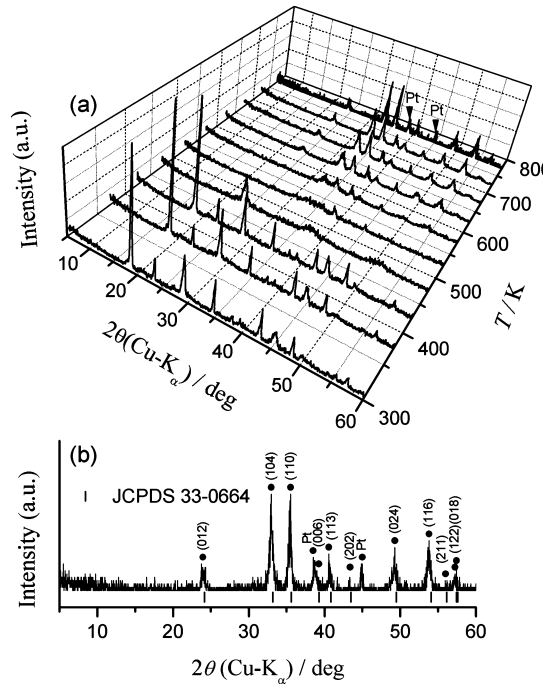

Figure 5. Changes of the XRD pattern of $FeC_2O_4 \cdot 2H_2O$ during stepwise isothermal heating in flowing air (a) and the XRD pattern of the final product at 773 K (b).

thermal dehydration, see Figure 6a,b, the absorption peak of C−O symmetric stretching at 1361 cm^{-1} [19,25−28] is diminished and that of the C−O asymmetric stretching at 1651 cm^{-1} is separated into two distinguished peaks at 1632 and 1664 cm^{-1}, in addition to the attenuation of the O−H stretching band at 3319 cm^{-1}. The product of the second mass-loss step indicates the trace of oxalate ion by the C−O asymmetric stretching bands at 1632 and 1664 cm^{-1}, see Figure 6c. The Fe−O vibration band observed for the crystalline hydrate and the dehydrated sample at 534 cm^{-1} disappears in the solid product of the second mass-loss step, indicating the poorly crystalline feature. The absorption due to the Fe−O vibration at 540 cm^{-1} appears again in the final product of the thermally induced transformation, see Figure 6d.

The particle morphologies and textures of the intermediate and final products are compared in Figure 7. It is clearly seen

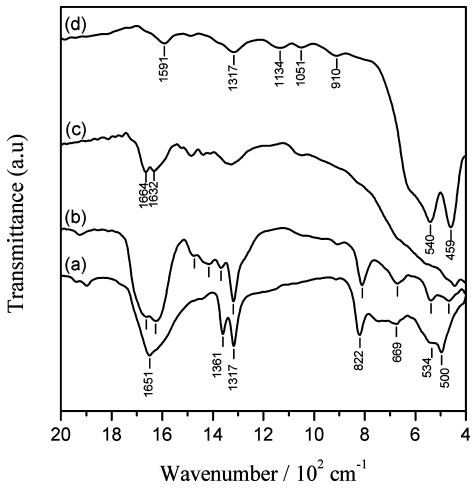

Figure 6. FT-IR spectra of the samples at the respective reaction stages. (a) $FeC_2O_4 \cdot 2H_2O$, (b) dehydration product produced by heating isothermally at 433 K for 5 h, (c) oxidative decomposition product by heating isothermally at 458 K for 5 h, and (d) crystallization product by heating linearly to 723 K.

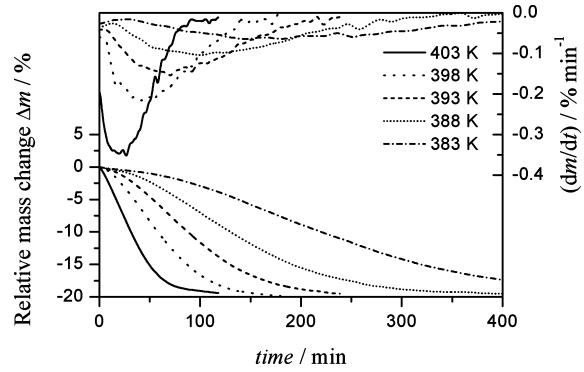

Figure 8. Isothermal mass-loss traces for the thermal dehydration process of $FeC_2O_4 \cdot 2H_2O$ at various temperatures in flowing air.

that the original particle shape and size are retained throughout the course of thermally induced transformation of the sample. After the thermal dehydration, the superficial cracking is developed in the restricted direction of the long axis of the original crystallite, Figure 7b. The cracks are further developed on the subsequent reaction steps, where the texture of glued prismatic bar is observed for the respective particles.

3.2. Thermal Dehydration. From the above findings, it is apparent that the first mass-loss step is the thermal dehydration of crystalline water as has been reported.[9−23] Figure 8 shows the isothermal mass-loss traces at various temperatures for the thermal dehydration process recorded under flowing air. The observed mass-loss value was $20.02 \pm 0.05\%$, which is closely corresponding to the value calculated by assuming the following equation

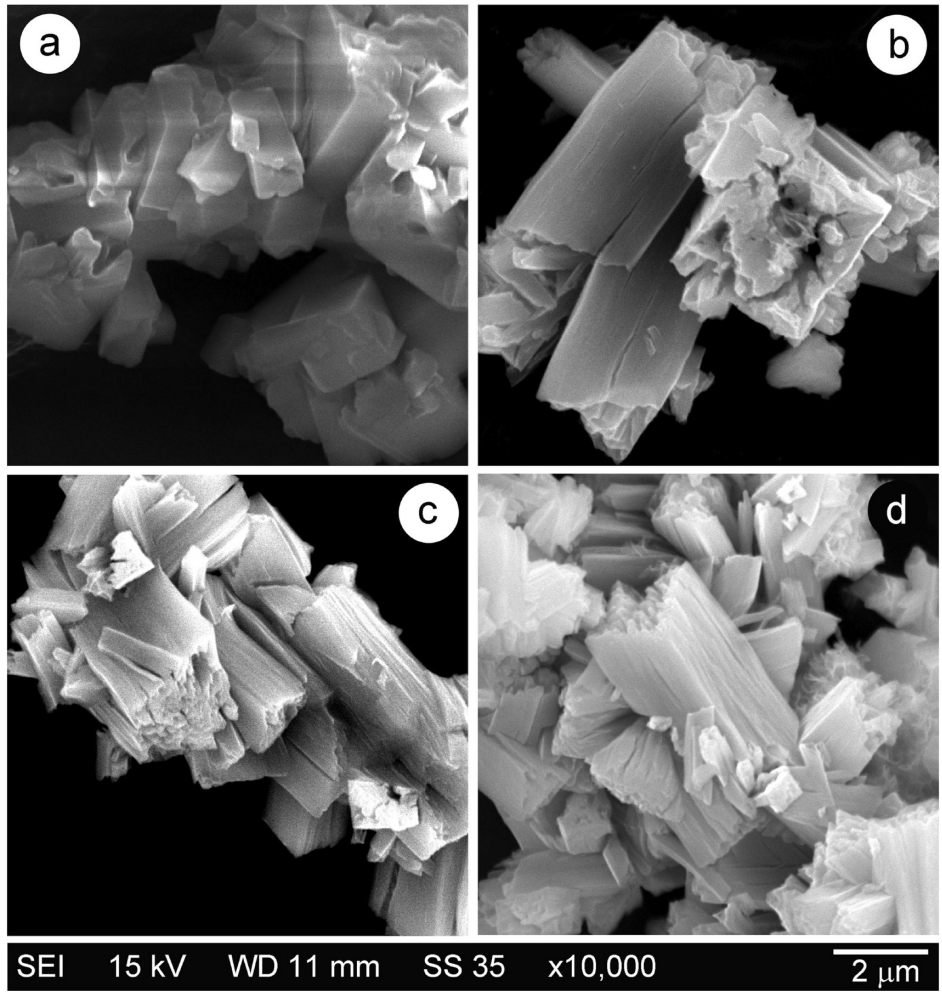

Figure 7. Typical SEM images of the samples at the respective reaction stages. (a) $FeC_2O_4 \cdot 2H_2O$, (b) dehydration product produced by heating isothermally at 433 K for 5 h, (c) oxidative decomposition product by heating isothermally at 458 K for 5 h, and (d) crystallization product by heating linearly to 723 K.

$$FeC_2O_4 \cdot 2H_2O \rightarrow FeC_2O_4 + 2H_2O \quad (1)$$

Changes of the XRD pattern during heating isothermally at 433 K under flowing air are shown in Figure 9, together with the detailed XRD pattern of the final dehydration product obtained by heating at 433 K for 6 h, Figure 9b. The diffraction peaks attributed to β-$FeC_2O_4 \cdot 2H_2O$ of the orthorhombic phase are attenuating gradually. Instead, the diffraction peak at $2\theta = 23.86°$ grows. Many of the diffraction peaks of the final product of the thermal dehydration, Figure 9b, are in agreement with the reported XRD pattern of anhydrous FeC_2O_4,[9,30] but some of major diffraction peaks are missing for the present anhydrous FeC_2O_4. This may be due to the poorly crystalline characteristic of the dehydration product.

It should be noted here that the reaction temperature of the thermal dehydration shifted to the higher temperatures in the high temperature XRD measurements with reference to the reaction in the measurements of isothermal mass-loss traces. This is likely due to the different sampling for the respective measurements. For the sample press-fitted on the platinum plate for the measurements of high temperature XRD, the gross diffusion of the evolved water vapor seems to be difficult producing the higher self-generated water vapor pressure in the reaction atmosphere, which prevent the forward reaction from the point of chemical equilibrium. Similarly, we have confirmed in advance that the onset temperature of the TG curve recorded at a heating rate shifts significantly to the high temperature when using more than 15 mg of sample weighed into the platinum cell (6 mmϕ and 3 mm in height). This is also due to the influence of the mass-transfer phenomena of the evolved gas as observed for the reversible decomposition reaction of solids.[31] Recently, Angermann and Töpfer reported the TG-DTA curves for the thermal decomposition of β-$FeC_2O_4 \cdot 2H_2O$ in air and in CO_2/CO mixture,[23] where the TG curve for the thermal dehydration in CO_2/CO mixture was observed at the higher temperatures. Similar behavior can be seen in the TG-differential thermogravimetry (TG-DTG) curves for $FeC_2O_4 \cdot 2H_2O$ recorded in air and in Ar.[16] These indicate the possibility of significant influence of oxygen partial pressure on the reaction temperature and kinetics of the thermal dehydration process, as well as on the nanocrystalline characteristics of the dehydration product.

Using the series of isothermal mass-loss traces in Figure 8, the kinetic analysis for the thermal dehydration of crystalline hydrate was performed as shown in Figure 10. The apparent activation energies, E_a, were calculated at the selected fractional reactions, α, by the Friedman method[32] according to the following equation

$$\ln\left(\frac{d\alpha}{dt}\right) = \ln[Af(\alpha)] - \frac{E_a}{RT} \quad (2)$$

where A and $f(\alpha)$ are the pre-exponential factor of Arrhenius equation and the kinetic model function of solid-sate reactions in differential form, respectively. The Friedman plots at various α from 0.1 to 0.9 in steps of 0.1 were shown in Figure 10a. At all the selected α, the plots of $\ln(d\alpha/dt)$ against T^{-1} line up on the respective straight lines, where the correlation coefficients of linear regression analysis are better than -0.99 in a wide range of α from 0.03 to 0.94. Figure 10b shows the values of E_a calculated from the slopes of the Friedman plots at different α. A systematic decrease of the value is observed for the early stage of the reaction, $\alpha < 0.1$, followed by the nearly constant values for the established reaction. The value of E_a averaged

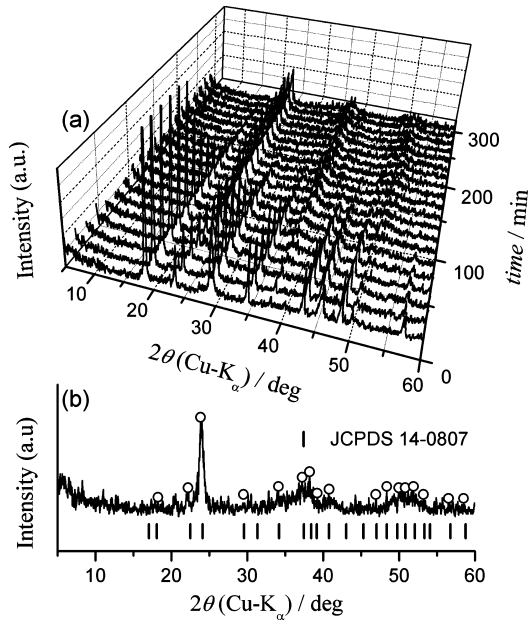

Figure 9. Changes of the XRD pattern during the isothermal dehydration process of $FeC_2O_4 \cdot 2H_2O$ at 433 K in flowing air (a) and the XRD pattern of the final dehydration product (b).

over $0.1 \leq \alpha \leq 0.9$ was 110.4 ± 5.4 kJ mol^{-1}. The constant E_a value over a wide range of α observed is satisfying the prerequisite of the fundamental kinetic equation assumed in eq 2. A kind of experimental master plots for the thermal dehydration was drawn by extrapolating the rate data to infinite temperature according to the following equation[33−35]

$$\left(\frac{d\alpha}{d\theta}\right)_\alpha = \left(\frac{d\alpha}{dt}\right)_\alpha \exp\left(\frac{E_a}{RT}\right) \qquad \text{with } \theta = \int_0^t \exp\left(-\frac{E_a}{RT}\right)dt \quad (3)$$

where θ is Ozawa's generalized time[36,37] denoting the simulated reaction time at infinite temperature. The experimental master plot of $(d\alpha/d\theta)$ against α is shown in Figure 10c. For correlating the experimental master plot with $f(\alpha)$, eq 3 can be rewritten as follows[33−35]

$$\left(\frac{d\alpha}{d\theta}\right) = Af(\alpha) \quad (4)$$

Superficially, the experimental master plot with a maximum on the way of reaction indicates the nucleation and growth type. According to eq 4, the most appropriate $f(\alpha)$ to describe the physico-geometric characteristics of the reaction mechanism[38,39] and the value of A were estimated through the nonlinear regression analysis by applying the Levenberg−Marquardt optimization algorithm.[40,41] The empirical function of Šesták−Berggren model,[42] SB(m, n, p): $f(\alpha) = \alpha^m(1-\alpha)^n[-\ln(1-\alpha)]^p$, which fits to various physico-geometric types of reaction and those deviated cases,[41,43,44] was employed for the model fitting, together with the typical nucleation−growth type model, that is Johnson−Mehl−Avrami−Erofeyev−Kolgomorov model JMA(m):[39,45] $f(\alpha) = m(1-\alpha)[-\ln(1-\alpha)]^{1-1/m}$. As can be seen from the fitting lines drawn in Figure 10c, the experimental master plot is fitted nearly perfectly by JMA(1.78) and SB(−1.15,1.38, 1.52). The comparable good fitting by SB(−1.15, 1.38,1.52) and JMA(1.78) supports the validity of JMA(1.78) as the appropriate model function describing the phsycio-geometric

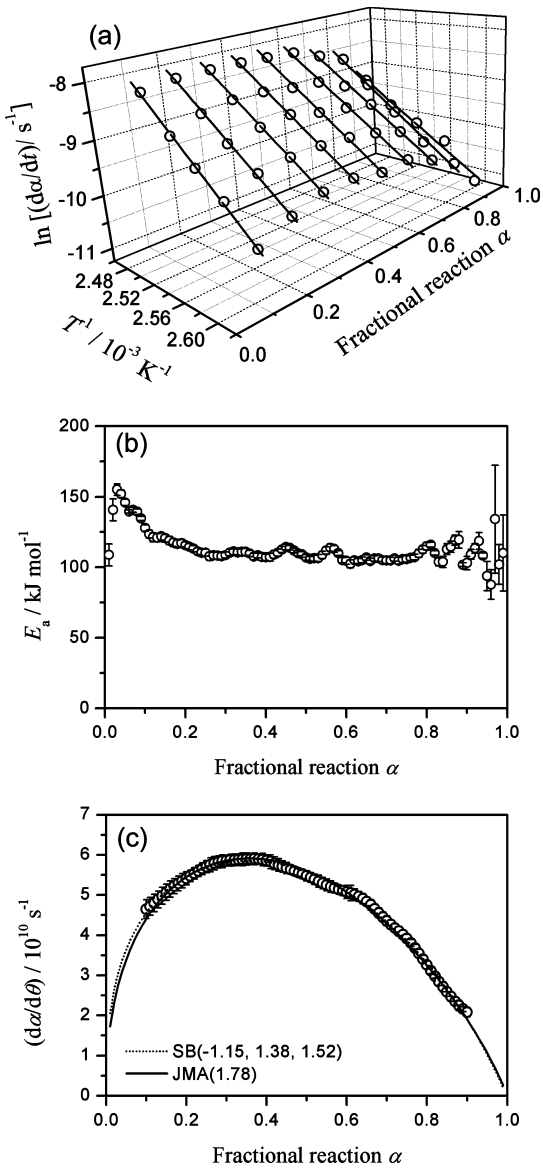

Figure 10. Kinetic analysis of the thermal dehydration process of $FeC_2O_4 \cdot 2H_2O$. (a) Friedman plots at different α, (b) the values of E_a at various α, and (c) comparisons of the experimental master plot with the theoretical curves of JMA(*m*) and SB(*m*, *n*, *p*) models.

characteristics of the process, even if the physical meanings of the kinetic exponents in SB(*m*, *n*, *p*) were difficult to interpret due to the large flexibility of these three parameters. The results of above formal kinetic analysis were summarized in Table 1.

Considering the thermal dehydration of a single crystalline particle, it is generally accepted that the reaction initiates on the surfaces by nucleation and subsequently proceeds by the advancement of reaction interface.[46−49] On the surface, the reaction rate is accelerated by the expansion of the reaction interface followed by the deceleration due to overlapping of the reaction interfaces growing from different initial nucleation sites. After being covered, the original reactant surface by the solid product layer, advancement of the reaction interface between the outer layer of solid product and the internal reactant crystal toward the center of reactant crystal regulates the reaction rate. Because of the shrinkage of the reaction interface as reaction advances, the reaction is decelerated. For the reaction where the surface reaction is contributing in a considerable portion of the overall reaction, the remarkable acceleration stage is observed in the early stage of the reaction. The kinetics of the surface reaction is usually described by the kinetic parameters different from those of the established reaction, because the nucleation is the independent kinetic process from growth[50,51] and the surface process is advantageous due to the energetic instability of the surface and the immediate diffusion of the evolved gas. On the other hand, when the contribution of the surface reaction on the overall reaction is negligible, the surface reaction is completed immediately and the established reaction proceeds decelerately by the shrinkage of reaction interface inward. Even if the rate behavior of a single particle is the decelerate process of interface shrinkage type, the overall rate behavior of the sample particles indicate apparently the nucleation and growth type when a large distribution of fractional reaction of the respective particles is existing among the sample particles.[52−54] Such situation is generated when the initiation time of the reaction and/or the particle size are distributing largely among the reactant particles. It should be noted here that, even in such situation, the apparent values of E_a evaluated by an isoconversional method correspond to those for the overall kinetic processes of the reaction interface advancement.[52−54]

In this schema, the present kinetic results indicate the contribution of the surface reaction in the early stage of the reaction because of the systematic decrease in the apparent E_a values in the range $\alpha < 0.1$. At the same time, it is also expected from the established reaction with the maximum reaction rate at $\alpha = 0.37$ that a distribution of fractional reactions among the reactant particles is existing. This is also supported by the size distributions of the reactant particles and the aggregate of these particles. It is very probable that the anhydrous FeC_2O_4 particles of pseudomorphic with the original reactant particles are constructed by the aggregates of the nanosized particles covered by the outer shell of the surface product layer.

3.3. Oxidative Decomposition of Anhydrous FeC_2O_4. Because the final solid product is α-Fe_2O_3 and the evolved gas during the second and third mass-loss steps is only CO_2, the following equation can be drawn for the total chemical reactions during the second and third mass-loss steps

$$2FeC_2O_4 + \frac{3}{2}O_2 \rightarrow Fe_2O_3 + 4CO_2 \qquad (5)$$

The total mass-loss value of the three steps averaged over the results of seven TG-DTA runs from room temperature to 773 K in air was 55.67 ± 0.32%, which is in good agreement with the calculated value of 55.6% for the total mass-loss due to eqs 1 and 5. Hypothetically, the oxidative decomposition of eq 5 can be constructed with three consecutive and/or concurrent processes as follows

$$FeC_2O_4 \rightarrow FeO + CO_2 + CO \qquad (6)$$

$$2FeO + \frac{1}{2}O_2 \rightarrow Fe_2O_3 \qquad (7)$$

$$CO + \frac{1}{2}O_2 \rightarrow CO_2 \qquad (8)$$

Equation 6 has been assumed as the initial reaction of oxalate ion break down in inert or reducing gas atmospheres,[9−14,17] where the reaction is endothermic. In contrast, eqs 7 and 8 are the exothermic processes, resulting in the exothermic behavior during the second mass-loss step, see Figure 4. At the second

TABLE 1: Results of Kinetic Analyses for the Respective Reaction Steps of the Thermally Induced Transformation of $FeC_2O_4 \cdot 2H_2O$ in Flowing Air

reaction step	E_a/kJ mol^{-1} (range of α)	kinetic model (range of α)	kinetic exponents	A/s^{-1}	$\gamma^{2\,a}$
thermal dehydration	110.4 ± 5.4 (0.10 ≤ α ≤ 0.90)	JMA(m) (0.10 ≤ α ≤ 0.90)	$m = 1.78 \pm 0.01$	$(7.38 \pm 0.03) \times 10^{10}$	0.9925
		SB(m, n, p) (0.10 ≤ α ≤ 0.90)	$m = -1.15 \pm 0.43$ $n = 1.38 \pm 0.17$ $p = 1.52 \pm 0.42$	$(1.14 \pm 0.04) \times 10^{11}$	0.9945
oxidative decomposition	131.0 ± 2.8 (0.12 ≤ α ≤ 0.89)	JMA(m) (0.10 ≤ α ≤ 0.20)	$m = 0.85 \pm 0.01$	$(1.30 \pm 0.02) \times 10^{11}$	0.9805
		JMA(m) (0.20 ≤ α ≤ 0.90)	$m = 1.11 \pm 0.01$	$(1.51 \pm 0.01) \times 10^{11}$	0.9984
		SB(m, n, p) (0.20 ≤ α ≤ 0.90)	$m = -0.72 \pm 0.54$ $n = 1.41 \pm 0.19$ $p = 0.89 \pm 0.51$	$(1.82 \pm 0.10) \times 10^{11}$	0.9996
crystallization	147.7 ± 7.4 (0.10 ≤ α ≤ 0.90)	JMA(m) (0.10 ≤ α ≤ 0.90)	$m = 1.26 \pm 0.03$	$(2.11 \pm 0.03) \times 10^{9}$	0.9265
		SB(m, n, p) (0.10 ≤ α ≤ 0.90)	$m = 2.49 \pm 0.30$ $n = 0.88 \pm 0.12$ $p = -1.80 \pm 0.29$	$(6.96 \pm 0.13) \times 10^{9}$	0.9997

[a] Square of correlation coefficient of the nonlinear regression analysis for (dα/dθ) vs α.

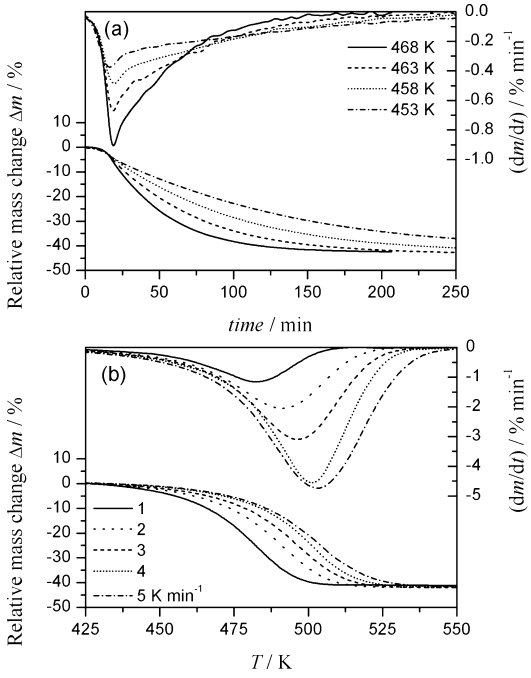

Figure 11. Mass-loss traces for the oxidative decomposition of anhydrous FeC_2O_4 in flowing air at several constant temperatures (a) and at different heating rates (b).

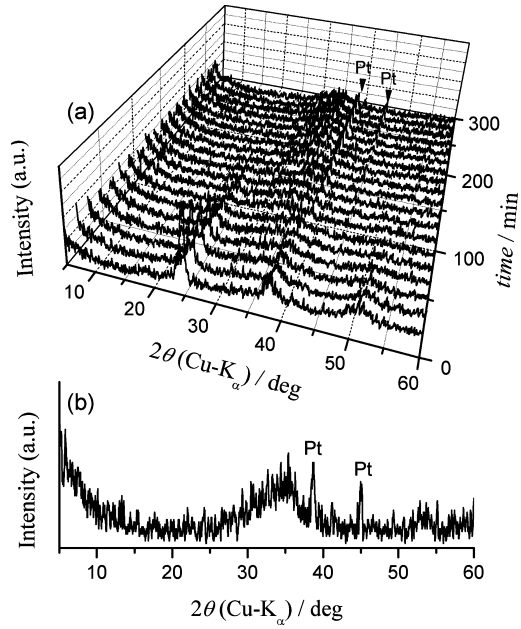

Figure 12. Changes of the XRD pattern during the oxidative decomposition process of anhydrous FeC_2O_4 at 448 K in flowing air (a) and the XRD pattern of the solid product after heating for 300 min (b).

mass-loss step, the kinetic processes at the reaction interface are thus influenced more or less by the self-heating effect.

Figure 11 shows the mass-loss curves for the oxidative decomposition of anhydrous FeC_2O_4 at several constant temperatures, Figure 11a, and under linearly increasing temperatures at different β, Figure 11b. The observed mass-loss value for the second mass-loss step is 41.97 ± 0.54% with reference to anhydrous FeC_2O_4, which is smaller by 2.54% than that of the calculated value according to eq 5. Changes of the XRD pattern during heating anhydrous FeC_2O_4 isothermally at 458 K is shown in Figure 12, together with the detailed XRD pattern of the final product of the second mass-loss step obtained by heating at 458 K for 6 h, Figure 12b. The diffraction peaks of anhydrous FeC_2O_4 disappear gradually with time, where no alternative peak appears. The poorly crystalline product of oxidative decomposition indicates the XRD hallow centered at around $2\theta = 35°$, which is in good agreement with those reported as amorphous Fe_2O_3 nanopowders produced during the thermal decomposition of the present sample[20] and other iron compounds, for example, $Fe_4[Fe(CN)_6]_3$.[8] Figure 13 shows the change of molar fraction of Fe^{3+} ion with respect to the total iron ions during heating the sample of $FeC_2O_4 \cdot 2H_2O$ at 468 K in flowing air. The induction period is observed as in the isothermal mass-loss traces in Figure 11a. The oxidation of Fe^{2+} ion is initiating at around 15 min and advancing with a decelerate behavior. The oxidation behavior is qualitatively

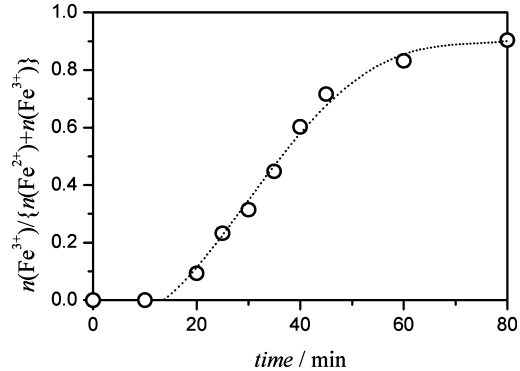

Figure 13. Change of molar fraction of Fe^{3+} ion with respect to the total iron ions during heating the sample of $FeC_2O_4 \cdot 2H_2O$ at 468 K in flowing air.

corresponding to the rate behavior of the oxidative decomposition evaluated by the isothermal mass-loss traces for the second mass-loss step, indicating the immediate oxidation of Fe^{2+} ion after the thermal decomposition of oxalate ion. From the above, the process of oxidative decomposition of the second mass-loss step is distinguished as the formation process of the amorphous Fe_2O_3 nanopowders. However, the product particles at this stage are pseudomorphic with the original sample particles with developing the cracks along the long axis of the rectangular, Figure 7c. The construction of the texture retaining the external form of the original sample is likely responsible for the arrest of the oxidative decomposition at the final stage. Thus, the particle shape and morphology of the original sample particles and/or those of the dehydrated intermediate may influence largely on the kinetic process of the oxidative decomposition. This has been demonstrated already by comparing the thermally induced transformation of the samples with different particle size and shape.[15] At the same time, it is very probable that the residual anhydrous FeC_2O_4 is playing a role of stabilizing the amorphous Fe_2O_3 nanopowders by confinement, as is observed for the stabilization of various amorphous and/or metastable polymorph phases.[55,56] This is also supported by the evolution of CO_2 during the third mass-loss step, being accompanied by the crystallization of α-Fe_2O_3, see Figure 4.

Figure 14 illustrates the kinetic analysis of the formation process of amorphous Fe_2O_3 nanopowders using the mass-loss traces recorded under isothermal and linearly increasing temperatures, that is, Figure 11. At various restricted α, all the data points measured under isothermal and linearly increasing temperatures line up on the straight lines on the coordinate of $\ln(d\alpha/dt)$ against T^{-1} as can be seen in Figure 14a. The Friedman plots at various selected α indicate good linearity in the wide range $0.12 \leq \alpha \leq 0.98$ with the correlation coefficient better than -0.99. The apparent values of E_a calculated from the slop of the Friedman plots at various α from 0.01 to 0.99 in steps of 0.01, see Figure 14b, indicate the linear increase from ca. 50 to 130 kJ mol^{-1} in the early stage of the reaction, $\alpha \leq 0.12$, followed by the exactly constant value of 131.0 ± 2.8 kJ mol^{-1} for the established part of the reaction in $0.12 \leq \alpha \leq 0.89$. The experimental master plot of $(d\alpha/d\theta)$ against α for the established part of the reaction is shown in Figure 14c. The change in the rate behavior at around $\alpha = 0.2$ can be clearly seen from the bend of the master plot. The initial decelerate part is fitted by JMA(0.85), where the kinetic exponent $m \leq 1$ indicates the nucleation and growth controlled by diffusion. The established part is fitted by JMA(1.11) supported by the similar good fitting by the empirical SB(-0.72,1.41,0.89). The kinetic results are summarized in Table 1.

Because the thermal decomposition of anhydrous FeC_2O_4 in an inert gas, reducing gas, or self-generated gaseous atmosphere takes place at the temperatures higher by ca. 200 K than the oxidative decomposition in air,[14,16,17,21,23] it is apparent that the rate behavior of the oxidative decomposition of anhydrous FeC_2O_4 is influenced largely by the change in the partial pressure of oxygen at the reaction sites. Because the reactant particles are retaining the external shape and size of the original particles of hydrated FeC_2O_4, it is expected by considering the contact with the atmospheric oxygen and the diffusion of the product gases that the oxidative decomposition is also initiating on the surface of the reactant particles. The systematic increase in the value of E_a and the diffusion controlled rate behavior observed for the initial part of the reaction ($\alpha \leq 0.2$) seem to result from possible decrease in the partial pressure of oxygen at the reaction sites due to the consumption of oxygen by the reaction and

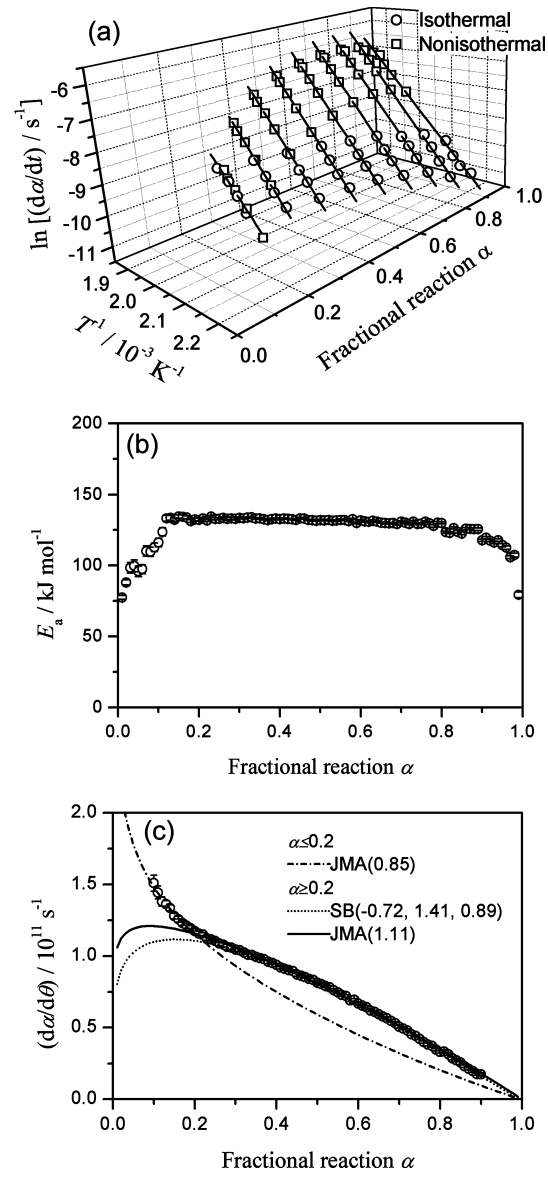

Figure 14. Kinetic analysis of the oxidative decomposition process of anhydrous FeC_2O_4. (a) Friedman plots at different α, (b) the values of E_a at various α, and (c) comparisons of the experimental master plot with the theoretical curves of JMA(m) and SB(m, n, p) models.

increase in the geometrical restriction of the oxygen diffusion to the reaction interfaces as reaction advances. It is also expected that the outer shell to retain the external form of the reacting particles is reconstructed through the surface reaction, where the surface cracks developed, see Figure 7c, are to be possible channels of the diffusion of oxygen to the reaction sites and the counter diffusion of gaseous products to out of the reaction system. The pseudofirst order rate behavior observed for the established part of the oxidative decomposition ($\alpha \geq 0.2$) is likely just overall behavior of the reaction, because the rate behavior is influenced largely by the gaseous diffusions and by the self-heating effect.

3.4. Crystallization of Amorphous Fe_2O_3. The detectable exothermic DTA peak observed after completing the second mass-loss step, see Figure 4, has been interpreted as is corresponding to the crystallization of amorphous Fe_2O_3 to α-Fe_2O_3.[22,23] The transformation is also confirmed in the present study by the change in the XRD patterns in the temperature range corresponding to the exothermic DTA peak, see Figure 5. Although no clear description can be found in the previous

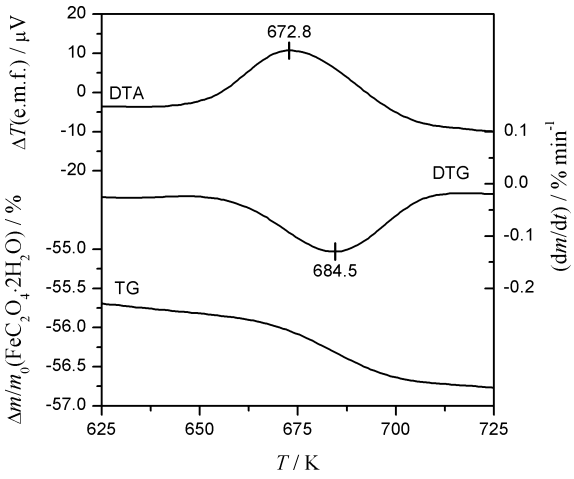

Figure 15. TG-DTG-DTA curves in the temperature range of the third mass-loss step with exothermic behavior recorded at $\beta = 5$ K min^{-1} in flowing air.

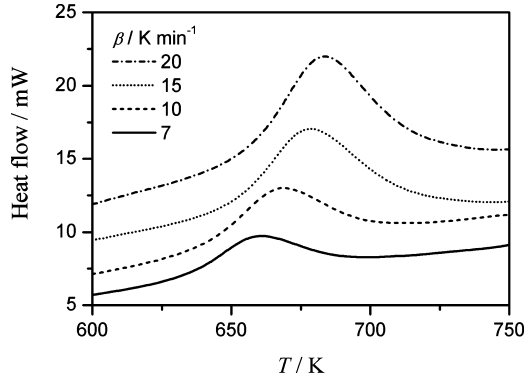

Figure 16. DSC curves for the exothermic process, accompanying the third mass-loss step, recorded at different β in flowing air.

articles, it should be noted that the exothermic DTA peak is accompanying the detectable mass-loss due to the oxidative decomposition of residual FeC_2O_4 assigned as the third mass-loss step in the present study. Because the oxidative decomposition of FeC_2O_4 is exothermic process, the exothermic DTA peak results from the overlapped processes of the crystallization of amorphous Fe_2O_3 and the oxidative decomposition of the residual FeC_2O_4. Figure 15 shows the TG-DTG-DTA curves in the temperature range of the third mass-loss step with exothermic behavior recorded at $\beta = 5$ K min^{-1} in flowing air. By comparing the DTA and DTG peaks, the DTG peak is observed at the higher temperatures indicating that the oxidative decomposition of residual FeC_2O_4 is induced by the crystallization of amorphous Fe_2O_3.

Figure 16 shows the DSC curves for the exothermic process, accompanying with the third mass-loss step, recorded at different β in flowing air. The apparent enthalpy change calculated from the DSC curves was -34.3 ± 1.6 kJ (mol Fe_2O_3)$^{-1}$. The formal kinetic analysis was performed using the DSC curves as shown in Figure 17. Apparently, the isoconversional relationship of eq 2 is established at various α as is seen from the Friedman plots in Figure 17a. The apparent values of E_a at various α calculated from the slopes of the Friedman plots are nearly constant with 147.7 ± 7.4 kJ mol^{-1} in the range $0.1 \leq \alpha \leq 0.9$, but increasing systematically in the range $\alpha > 0.2$, see Figure 17b. In the final part of the exothermic peak ($\alpha \geq 0.8$), the E_a value is raising up extensively. Figure 17c shows the experimental master plot of $(d\alpha/d\theta)$ against α drawn in a perfunctory way by assuming a single rate process with the constant E_a

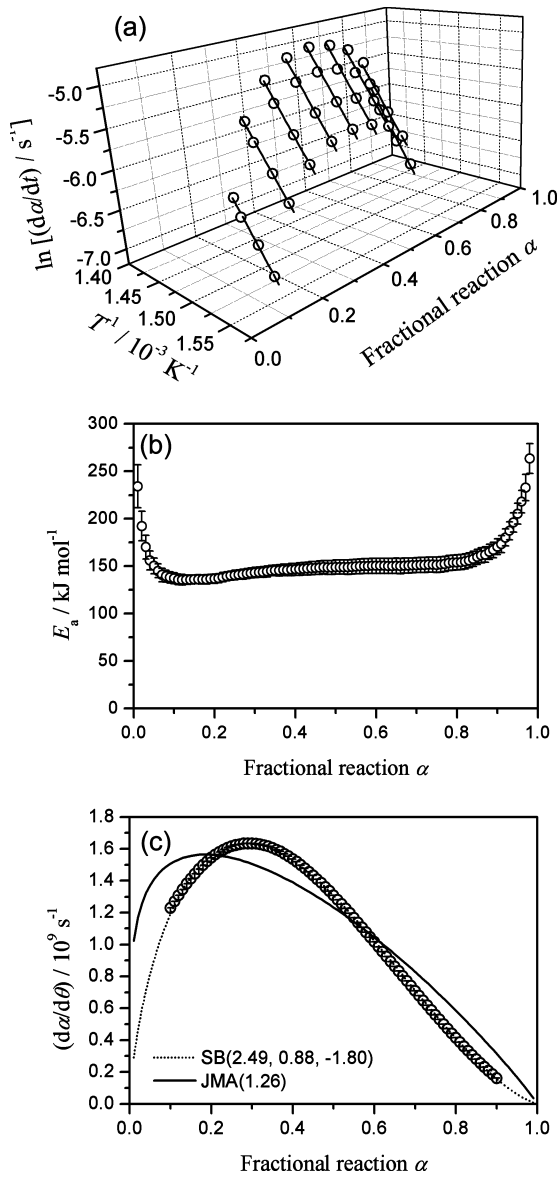

Figure 17. A formal kinetic analysis of the overlapped processes of crystallization of amorphous Fe_2O_3 and oxidative decomposition of residual FeC_2O_4. (a) Friedman plots at different α, (b) the values of E_a at various α, and (c) comparisons of the experimental master plot with the theoretical curves of JMA(m) and SB(m, n, p) models.

value. From the microscopic observation of the crystallization of amorphous Fe_2O_3 to α-Fe_2O_3 reported by Hermanek et al.,[22] it is apparent that the crystallization process is controlled kinetically by the nucleation of α-Fe_2O_3 and subsequent growth of the nuclei. Although the experimental master plot indicates the maximum rate on the way of the process at $\alpha = 0.29$, the concaved shape of the rate behavior observed in the second half of the process is apparently different from the ideal master curve of the nucleation and growth type. The best fitting by a model function of nucleation and growth type was observed for JMA(1.26), but the fitting curve was deviated largely from the experimental master plot as shown in Figure 17c. The kinetic results of the above formal curve fitting were also listed in Table 1.

The apparent kinetic behavior, characterized by the maximum rate at $\alpha = 0.29$ with systematic increase in the E_a value in the range $\alpha > 0.2$ and the concaved shape of the rate behavior in the second half of the process accompanied by the drastic increase in the E_a value at the end of the overall reaction,

supports qualitatively the interpretation of the exothermic phenomenon deduced from the TG-DTG-DTA curves in Figure 16, that is, the phenomenon results from an overlapped process of the crystallization of amorphous Fe_2O_3 and the oxidative decomposition of residual FeC_2O_4 induced by the crystallization of Fe_2O_3. The systematic increase of E_a value in the range $\alpha > 0.2$ is likely the apparent result from the participation of the oxidative decomposition of the residual FeC_2O_4 to the preceding crystallization of amorphous Fe_2O_3. The concave-shaped rate behavior in the second half of the overall process with the drastic increase in E_a at the end can be explained by the ending of the crystallization process and the reaction tail of the oxidative decomposition. From the kinetic behavior of the previous oxidative decomposition step, the reactant particles of this step seems to be constructed by internal phases of the amorphous Fe_2O_3 and residual FeC_2O_4 protected by the outer shell of surface amorphous Fe_2O_3 layer. It is expected that the crystallization of the amorphous Fe_2O_3 on the particle surfaces will be the trigger of the crystallization of internal amorphous Fe_2O_3 and the oxidative decomposition of residual FeC_2O_4. As can be seen in Figure 7d, the final solid product, α-Fe_2O_3, is still retaining the external form of the original reactant particles, $FeC_2O_4 \cdot 2H_2O$, with further development of surface cracks, indicating the formation and reconstruction of the surface product layer at the respective reaction steps play important roles to control the physico-geometric kinetics of the thermal decomposition of $FeC_2O_4 \cdot 2H_2O$ in flowing air.

4. Conclusions

The final product of α-Fe_2O_3 is produced by the thermally induced transformation of $FeC_2O_4 \cdot 2H_2O$ in air through three distinguished reaction steps of the thermal dehydration of the crystalline hydrate, the oxidative decomposition of anhydrous FeC_2O_4, and the crystallization of amorphous Fe_2O_3. The external shape of the reactant particles is retained throughout the reaction processes, accompanied by the stepwise developments of the superficial cracks in the restricted direction of the long axis of the original crystals. The outer shell of the surface product layer of the reacting particles, developed or reconstructed in the respective reaction steps, play important role to retain the pseudomorphic shape of the reacting particles. The initial parts of the respective reaction steps are controlled by the development and/or reconstruction processes of the surface product layers. The outer shell of the surface product layers regulates the physico-geometry of the kinetic behavior of the established part of the respective reaction steps.

From the present kinetic study, the following reaction scheme can be drawn. The apparent overall rate behavior of the nucleation and growth type with $E_a = 110.4 \pm 5.4$ kJ mol^{-1} observed for the present thermal dehydration process is interpreted as resulting from the distribution of the fractional reactions among the reacting particles caused by the possible time distribution of the nucleation on the surface and/or by the remarkable size distribution of the reactant particles. The oxidative decomposition of dehydrated sample to produce the amorphous Fe_2O_3 is characterized by the diffusion controlled rate behavior observed in the initial part of reaction. The outer shell of the surface product layer regulates the gaseous diffusion of reactant oxygen into the internal of the particles and the counter diffusion of the product gases to the external of the particles, representing the apparent rate behavior of pseudofirst order reaction with $E_a = 131.0 \pm 2.8$ kJ mol^{-1}. The outer shell impedes the oxidative decomposition at the final stage of the reaction, where the internal product of amorphous Fe_2O_3 may be stabilized in confinement by the outer shell of surface product layer and the internal residue of FeC_2O_4. The crystallization of the outer shell of amorphous Fe_2O_3 induces the crystallization of internal amorphous Fe_2O_3 and the oxidative decomposition of residual FeC_2O_4.

Acknowledgment. The present work was supported partially by a grant-in-aid for scientific research (B) (21360340 and 22300272) from Japan Society for the Promotion of Science.

References and Notes

(1) Cornell, R. M.; Schwertmann, U. *The Iron Oxides: Structure, Properties, Reactions, Occurrences and Uses*, 2nd ed.; Wiley-VCH: Weinhelim, 2003.
(2) Schwertmann, U.; Cornell, R. M. *Iron Oxides in the Laboratory: Preparation and Characterization*, 2nd ed.; Wiley-VCH: Weinhelim, 2000.
(3) Faivre, D.; Shüler, D. *Chem. Rev.* **2008**, *108*, 4875–4898.
(4) Koga, N.; Okada, S.; Nakamura, T.; Tanaka, H. *Thermochim. Acta* **1995**, *267*, 195–208.
(5) Koga, N.; Takemoto, S.; Nakamura, T.; Tanaka, H. *Thermochim. Acta* **1996**, *282/283*, 81–90.
(6) Pérez-Maqueda, L. A.; Criado, J. M.; Real, C.; Šubert, J.; Boháček, J. *J. Mater. Chem.* **1999**, *9*, 1839–1845.
(7) Chopra, G. S.; Real, C.; Alealá, M. D.; Pérez-Maqueda, L. A.; Šubert, J.; Criado, J. M. *Chem. Mater.* **1999**, *11*, 1128–1138.
(8) Zboril, R.; Machala, L.; Mashlan, M.; Sharma, V. *Cryst. Growth Des.* **2004**, *4*, 1317–1325.
(9) Brown, R. A.; Bevan, S. C. *J. Inorg. Nucl. Chem.* **1966**, *28*, 387–391.
(10) Macklen, E. D. *J. Inorg. Nucl. Chem.* **1967**, *29*, 1229–1234.
(11) Rao, V.; Shashimohan, A. L.; Biswas, A. B. *J. Mater. Sci.* **1974**, *9*, 430–433.
(12) Rane, K. S.; Nikumbh, A. K.; Mukhedkar, A. J. *J. Mater. Sci.* **1981**, *16*, 2387–2397.
(13) Boyanov, B.; Khadzhiev, D.; Vasilev, V. *Thermochim. Acta* **1985**, *93*, 89–92.
(14) Mohamed, M. A.; Galwey, A. K. *Thermochim. Acta* **1993**, *213*, 269–278.
(15) Chhabra, V.; Lal, M.; Maitra, A. N.; Ayyub, P. *Colloid Polym. Sci.* **1995**, *273*, 939–946.
(16) Rupard, R. G.; Gallagher, P. K. *Thermochim. Acta* **1996**, *272*, 11–26.
(17) Carles, V.; Alphonse, P.; Tailhades, P.; Rousset, A. *Thermochim. Acta* **1999**, *334*, 107–113.
(18) Popa, M.; Calderon-Moreno, J. M.; Crisan, D.; Zaharescu, M. *J. Therm. Anal. Calorim.* **2000**, *62*, 633–645.
(19) Frost, R. L.; Weier, M. L. *J. Therm. Anal. Calorim.* **2004**, *75*, 277–291.
(20) Zboril, R.; Machala, L.; Mashlan, M.; Hermanek, M.; Miglierini, M.; Fojtik, A. *Phys. Stat. Sol. (c)* **2004**, *1*, 2583–3588.
(21) Hermanek, M.; Zboril, R.; Mashlan, M.; Machala, L.; Schneeweiss, O. *J. Mater. Chem.* **2006**, *16*, 1273–1280.
(22) Hermanek, M.; Zboril, R.; Medrik, I.; Pechousek, J.; Gregor, C. *J. Am. Chem. Soc.* **2007**, *129*, 10929–10936.
(23) Angermann, A.; Töpfer, J. *J. Mater. Sci.* **2008**, *43*, 5123–5130.
(24) Deyrieux, R.; Prnrloux, A. *Bull. Soc. Chim. Fr.* **1969**, *8*, 2675–2681.
(25) Bickley, R. I.; Edwards, H. G. M.; Rose, S. J. *J. Mol. Struct.* **1991**, *243*, 341–350.
(26) Frost, R. L.; Weier, M. L. *J. Raman Spectrosc.* **2003**, *34*, 776–785.
(27) Frost, R. L.; A. Locke; Martene, W. N. *J. Raman Spectrosc.* **2008**, *39*, 901–908.
(28) Echigo, T.; Kimata, M. *Phys. Chem. Minerals* **2008**, *35*, 467–475.
(29) JCPDS 33-0664.
(30) JCPDS 14-0807.
(31) Koga, N.; Criado, J. M. *Int. J. Chem. Kinet.* **1988**, *30*, 737–744.
(32) Friedman, H. L. *J. Polym. Sci. C* **1964**, *6*, 183–195.
(33) Ozawa, T. *J. Therm. Anal.* **1986**, *31*, 547–551.
(34) Koga, N. *Thermochim. Acta* **1995**, *258*, 145–159.
(35) Gotor, F. J.; Criado, J. M.; Malek, J.; Koga, N. *J. Phys. Chem. A* **2000**, *104*, 10777–10782.
(36) Ozawa, T. *Bull. Chem. Soc. Jpn.* **1965**, *38*, 1881–1886.
(37) Ozawa, T. *Thermochim. Acta* **1986**, *100*, 109–118.
(38) Koga, N.; Tanaka, H. *Thermochim. Acta* **2002**, *388*, 41–61.
(39) Khawam, A.; Flanagan, D. R. *J. Phys. Chem. B* **2006**, *110*, 17315–17328.
(40) Bates, D. M.; Watts, D. G. *Nonlinear Regression and its Application*: Wiley, New York, 1988.

(41) Koga, N.; Mako, A.; Kimizu, T.; Tanaka, Y. *Thermochim. Acta* **2008**, *467*, 11–19.
(42) Sestak, J.; Berggren, G. *Thermochim. Acta* **1971**, *3*, 1–12.
(43) Sestak, J. *J. Therm. Anal.* **1990**, *36*, 1997–2007.
(44) Perez-Maqueda, L. A.; Criado, J. M.; Sanchez-Jimenez, P. E. *J. Phys. Chem. A* **2006**, *110*, 12456–12462.
(45) Finney, E. E.; Finke, R. G. *Chem. Mater.* **2009**, *21*, 4692–4705.
(46) Tanaka, H.; Koga, N. *J. Phys. Chem.* **1988**, *92*, 7023–7029.
(47) Koga, N.; Tanaka, H. *J. Phys. Chem.* **1989**, *93*, 7793–7798.
(48) Galwey, A. K.; Koga, N.; Tanaka, H. *J. Chem. Soc., Faraday Trans.* **1990**, *86*, 531–537.
(49) Koga, N.; Tanaka, H. *J. Phys. Chem.* **1994**, *98*, 10521–10528.
(50) Jacobs, P. W. M. *J. Phys. Chem. B* **1997**, *101*, 10086–10093.
(51) Skrdla, P. J. *J. Phys. Chem. A* **2004**, *108*, 6709–6712.
(52) Koga, N.; Criado, J. M. *J. Therm. Anal.* **1997**, *49*, 1477–1484.
(53) Koga, N.; Criado, J. M. *J. Am. Ceram. Soc.* **1998**, *81*, 2901–2909.
(54) Koga, N.; Kimizu, T. *J. Am. Ceram. Soc.* **2008**, *91*, 4052–4058.
(55) Stephens, C. J.; Ladden, S. F.; Meldrum, F. C.; Christenson, H. K. *Adv. Funct. Mater.* **2010**, *20*, 2108–2115.
(56) Radha, A. V.; Forbes, T. Z.; Likkan, C. E.; Gilbert, P. U. P. A.; Navrotsky, A. *Proc. Natl. Acad. Sci. U.S.A.* **2010**, *107*, 16438–16443.

JP110407N